DInSAR measurements of ground deformation by sinkholes, mining subsidence, and landslides, Ebro River, Spain

Carmen Castañeda[1], Francisco Gutiérrez[2], Michele Manunta[3], and Jorge P. Galve[2]

[1]*Agricultural Research Center of Aragon (C.I.T.A.), Soils and Irrigation Department, Av. Montañana 930, 50059 Zaragoza, Spain. (ccastanneda@aragon.es)*

[2]*Earth Sciences Department, University of Zaragoza, c/. Pedro Cerbuna 12, 50009 Zaragoza, Spain. (fgutier@unizar.es)*

[3]*Institute for Electromagnetic Sensing of the Environment (I.R.E.A.-C.N.R.), Via Diocleziano 328, 80124 Naples, Italy (manunta.m@irea.cnr.it)*

Running Title: Evaporite deformation by DInSAR

Abstract

Differential Interferometric Synthetic Aperture Radar (DInSAR) has been applied to detect and measure ground deformation in a stretch of the Ebro River valley (Spain) excavated in salt-bearing evaporites. The capability of the Small Baseline Subset (SBAS) DInSAR technique to detect ground displacement is analyzed comparing the DInSAR results with the available geomorphological information. The deformation map derived from 27 European Remote Sensing (ERS) satellite images covering more than five years provides sub-centimeter displacement measurements in zones coinciding with known active sinkholes and landslides. Moreover the map provides the first account of mining subsidence in the area. The measured deformation rates reach 1.68 cm/y for the sinkholes, 0.80 cm/y for the landslides and 1.45 cm/y for the area affected by mining subsidence. The SBAS DInSAR technique provided deformation measurements in a small proportion (5-10%) of the known active sinkholes and landslides. This limitation is mainly due to the lack of coherence in agricultural areas, the spatial resolution of the deformation map (pixel size of 90 m), and the parallelism between the ERS satellite line of sight and the linear escarpment on which most of the landslides occur. Despite this, the interferometric technique provides valuable data that complement traditional geomorphological studies including the quantification of the deformation phenomena, the identification of mining subsidence otherwise only recognizable by geodetic methods, and the detection of creep deformation which might correspond to premonitory indicators of catastrophic sinkholes and landslides capable of causing the loss of lives. Detailed DInSAR studies combined with field data would be required to improve the analysis of each deformation area.

Key words: interferometry, subsidence, evaporites.

1. Introduction

An important aspect from the applied and scientific perspective is the study of the deformation of the Earth ground surface, including the identification of the areas affected by displacement, the measurement of the deformation magnitude and rate, the elucidation of the temporal strain regime (continuous vs. episodic) and the diagnosis of its origin. Active surface deformation may be related to endogenous processes (tectonic and volcanic activity), exogenous processes (landslides, dissolution-induced subsidence, compaction and consolidation of sediments, oxidation of organic deposits, thawing of ground ice) and anthropogenic activities (withdrawal of groundwater or hydrocarbons, excavation of underground cavities) (Waltham, 1989; Galloway *et al.*, 1999).

Geomorphic and stratigraphic markers with a known age and original geometry may be used to measure cumulative displacements and estimate mean deformation rates (Burbank and Anderson, 2001). The application of retrodeformation analysis and absolute dating techniques to deformed sediments exposed in trenches or natural outcrops may provide information on the style and chronological evolution of the ground deformation associated with faults (McCalpin, 1996), landslides (McCalpin and Hart, 2002; Gutiérrez *et al.*, 2008d) and sinkholes (Gutiérrez *et al.*, 2008b, 2009).

Most of the geodetic techniques, including GPS, allow measuring recent short-term ground deformation in a limited number of points. Conversely, differential SAR interferometry (DInSAR) is a space-based technique that allows detecting and measuring ground deformation over large areas with high spatial resolution and centimeter to millimeter accuracy. The technique is based on the measurement of the phase variation (interferometric phase) between successive radar acquisitions and requires the use of a digital elevation model to remove the altitude contribution from the interferometric phase. The ground displacements are calculated on the SAR sensor line of sight (LOS).

The technique was first applied to single deformation events such as ground motion in agricultural fields related to changes in the soil moisture caused by irrigation (Gabriel *et al.*, 1989) or ground displacement associated with the 1992 Landers, California earthquake (Massonet *et al.*, 1993). Subsequently, differential SAR interferometry has been used to study different types of surface deformation, including active faulting and preseismic, coseismic and postseismic displacements (Massonnet *et al.*, 1993; Pagli *et al.*, 2003; Sarti *et al.*, 2003; Fialko *et al.*, 2005), ground movement related to volcanic activity (Sigmudsson, 1999; Fernández *et al.*, 2003; Massonnet *et al.*, 2005), active landslides (Colesanti and Wasowski, 2006; Moro *et al.*, 2007), subsidence in urban areas (Crosetto *et al.*, 2003; Raucoules *et al.*, 2003a; Le Mouélic *et al.*, 2005; Cascini *et al.*, 2006), mining subsidence (Raucoules *et al.*, 2003b; Ge *et al.*, 2007; Herrera *et al.*, 2007), multiyear and seasonal uplift and subsidence controlled by groundwater withdrawal and recharge (Amelung *et al.*, 1999; Galloway *et al.*, 1998; Hoffman *et al.*, 2001), shrink-swell cycles in soils related to rainfall (Massonnet and Feigl, 1998), the identification and anticipation of sinkholes in karst areas (Baer *et al.*, 2002; Closson *et al.*, 2005; Ferretti *et al.*, 2004), surface water level changes in wetlands (Wdowinksky *et al.*, 2008), ground motion in response to water level and loading changes in reservoirs (Cavalié *et al.*, 2007), and surface changes and movement in glaciers (Goldstein *et al.*, 1993; Legresy *et al.*, 2000).

In contrast to the conventional DInSAR technique, based on individual SAR interferograms, in the last years several advanced DInSAR techniques (Ferretti *et al.*, 2001; Berardino *et al.*, 2002; Mora *et al.*, 2003; Usai, 2003; Werner *et al.*, 2003; Hooper *et al.*, 2004; Crosetto *et al.*, 2005; Kampes, 2005; Bovenga *et al.*, 2006; Hooper *et al.*, 2007) have been developed to generate deformation time series in order to study the temporal evolution of the detected displacements. Moreover, these advanced DInSAR techniques allow filtering and removing the atmospheric phase component by exploiting the high spatial and low temporal correlation (Ferretti *et al.*, 2000) of the troposphere heterogeneities between the different radar acquisitions (Tarayre and Massonet, 1996; Hanssen *et al.*, 1999; Hanssen, 2001).

These DInSAR approaches can be classified in two main categories, PS-like and coherence-based, depending on the type of detected scatterers. The PS-like approach (Ferretti *et al.*, 2001; Werner *et al.*, 2003; Kampes, 2005; Bovenga *et al.*, 2006) operates on single-look interferograms, generated with respect to a reference (master) image, without any constraint on the spatial and temporal baselines of the SAR data acquisition orbits. This strategy allows analyzing single targets, referred to as Persistent Scatterers (PS), that exhibit sufficiently stable radar reflectivity and are almost unaffected by temporal and spatial decorrelation.

The coherence-based approaches (Berardino *et al*., 2002; Mora *et al*., 2003; Usai, 2003; Hooper *et al*., 2004; Crosetto *et al*., 2005; Hooper *et al*., 2007) use an appropriate combination of averaged (multi-look) differential interferograms, characterized by relatively small spatial and temporal baselines, in order to reduce the decorrelation effects and detect not only PS but also distributed scatterers. Accordingly, these approaches allow maximizing the detected coherent pixel density.

The above mentioned advanced DInSAR techniques require a relatively large SAR acquisition dataset, typically more than 20 images, for analyzing slow ground deformation phenomena of the order of mm/y. Moreover, coherent conditions are required among radar acquisitions. Temporal decorrelation or incoherence, even for short time intervals, is mainly due to geometric and electric variations in the ground surface, the latter being mainly determined by changes in the water content of the soil and vegetation. High temporal coherence values are generally obtained for areas without dense vegetation and L-band (24-cm wavelength) instruments, less sensitive to small changes in scattering characteristics (Hanssen, 2001). In the ERS satellite case (C-band with a wavelength of about 5.65 cm), temporal decorrelation is highly dependent on the land covers. Urban and vegetation-free areas are the most suitable surfaces and areas affected by agricultural practices, erosion and aggradation, the main sources of the interferometric decorrelation, are the least suitable surfaces.

In this study, we have applied the Small BAseline Subset (SBAS) algorithm combining DInSAR interferograms (Berardino *et al*., 2002). This approach exploits averaged (multilook) small baseline interferograms (i.e. limited spatial and temporal separation between SAR image orbits) and allows studying very large areas, more than 100 km x 100 km (Casu *et al.*, 2008). The SBAS technique produces spatially dense ground mean deformation velocity maps of the analyzed area and displacement time series over the time period observed. Accordingly, it has been successfully applied on several areas affected by ground deformation due to volcanic (Borgia *et al.*, 2005; Manzo *et al.*, 2006) and tectonic activity (Berardino *et al.*, 2004; Lundgren *et al.*, 2004; Berardino *et al.*, 2007; Lanari *et al.*, 2007) and by seasonal and multi-year volume changes in exploited aquifer systems (Lanari *et al.*, 2004). Moreover, the SBAS approach has been effectively exploited to detect and monitor urban area deformation (Cascini *et al.*, 2006) with the potential to discriminate between the natural and antropogenic components of deformation (Stramondo *et al.*, 2007). Finally, a quality assessment of the technique (Casu *et al.*, 2006), showing subcentimeter accuracy, has been carried out by means of ground leveling and GPS measurements.

The aim of this work is to exploit the SBAS-DInSAR technique for detecting and quantifying different types of natural and human-induced ground deformation in a stretch of the Ebro River valley around Zaragoza city, NE Spain. In this area, dominated by outcrops of Tertiary evaporites partly covered by Quaternary alluvium, two types of ground deformation have been previously documented: (1) sinkholes caused by dissolution of the bedrock; (2) landslides in the escarpment located in the northern margin of the Ebro River valley.

The SBAS-DInSAR technique applied in this study is used to measure deformation rates in known sinkholes and landslides and to detect unknown subsidence over an active salt mine. A discussion on the advantages and limitations of the applied technique is provided by comparing the SBAS-DInSAR results with the data on sinkhole and landslide distribution and activity gathered by traditional geomorphological investigations (mainly aerial photograph interpretation and field surveys).

2. Geological Setting

The study area, covering about 60 km x 30 km, is located in the central sector of the Ebro Tertiary Basin in NE Spain (Figure 1). This geological unit, which constitutes the southern foreland basin of the Pyrenees, is longitudinally drained by the Ebro River following a WNW-ESE trend. In the sector analyzed in this contribution, the infill of the basin is composed of two main subhorizontally lying stratigraphic units deposited in lake environments surrounded by alluvial fan systems. The youngest unit, Middle Miocene in age, is the Alcubierre Limestone Formation (Quirantes, 1978; Pérez-Rivarés *et al.*, 2002, 2004). This formation, consisting of a resistant carbonate sequence 50-60 m thick, forms prominent mesas and structural reliefs on both flanks of the Ebro Valley reaching more than 600 m a.s.l. The older unit corresponds to the Zaragoza Gypsum Formation (Quirantes, 1978), which according to oil exploration boreholes locally reaches 850 m in thickness (Torrescusa and Klimowitz, 1990). This lithostratigraphic unit grades laterally into shales deposited in distal alluvial fan environments. The exposed upper 300 m of the Zaragoza Formation exhibit secondary gypsum layers with thin marl intercalations and shale units up to several tens of meters thick. The outcrops of the Zaragoza Formation are dominated by rounded gypsum hills with scarce xerophytic vegetation and a dense dendritic network of infilled valleys locally known as *vales* (Gutiérrez and Gutiérrez, 1998). Mining exploration boreholes performed near Zaragoza city reveal the presence of halite and glauberite units several tens of meters thick at shallow depth (Salvany *et al.*, 2007; Guerrero *et al.*, 2008a). A halite unit some 10 m thick crops out near Remolinos village at about 70-75 m above the Ebro River floodplain (Figure 1). This halite deposit, exploited since Roman times, is currently mined by the room and pillar method. The Tertiary bedrock, affected by vertical joints with prevailing WNW-ESE, N-S and E-W trends (Arlegui and Simón, 2001), displays a very gentle syncline whose axis coincides approximately with the trace of the Ebro River valley (Quirantes, 1978).

Once the endorheic Ebro Basin was captured by the external drainage network and opened to the Mediterranean Sea in Middle-Late Miocene times (García-Castellanos *et al.*, 2003; Pardo *et al.*, 2004), a new drainage network started to develop and dissect the infill of the basin (Gutiérrez and Gutiérrez, 1998). The entrenchment of the fluvial network, controlled by the trunk Ebro River, has been punctuated by periods of aggradation recorded by a stepped sequence of fluvial terraces and mantled pediments. A total of 11 terrace and 7 pediment levels has been mapped in the studied stretch of the Ebro Valley (Guerrero, 2008). The aggradation surface of the oldest preserved terrace is situated at 200-210 m above the Ebro River channel, which lies at 220-165 m a.s.l. in the study area.

(Figure 1)

The long-term migration of the Ebro River toward the NE has resulted in a markedly asymmetric valley, flanked by a stepped sequence of Quaternary alluvial levels in the southern margin and bounded by a prominent gypsum escarpment on the northern flank (Figure 1). This cliff, up to 180 m high, extends for more than 70 km and is interrupted by the Gállego River valley North of Zaragoza (Figure 1). Its rapid retreat is revealed by the presence of hanging valleys and conspicuous triangular facets. This gypsum escarpment, whose linear trace is controlled by the highly penetrative WNW-ESE trending joint set, displays numerous active and inactive slope movements (Pellicer *et al.*, 1984; Gutiérrez *et al.*, 1994) that reach more than 10 million m^3 in volume (Figure 2A). The typology of the landslides and their distribution is largely controlled by the lithostratigraphy of the Tertiary sediments forming the scarp (Gutiérrez *et al.*, 1994). Large rotational rock-slides, some with a lateral spreading component, occur preferentially in the sectors where shale units crop out at the base of the scarp (Figure 2A). Rock-topples, rock-falls and small rock-avalanches are the dominant mass movement types where the Tertiary succession is devoid of argillaceous units in the basal portion of the escarpment (Figure 2B). The development of landslides is favoured by the reduction in the rock mass strength caused by dissolution along fractures (joints and stress release cracks) and undermining of the escarpment by the river channel (Gutiérrez *et al.*, 1994; Guerrero *et al.*, 2004a). In fact, there is a good spatial correlation between the distribution of the active slope movements and the sectors where current or recently abandoned Ebro River channels are located at or close to the base of the scarp. At the present time, the interaction between the escarpment and the river occurs upstream of Zaragoza city, where most of the active landslides are located, whereas downstream a terrace separates the cliff from the Ebro River. Rock-falls derived from gypsum escarpments in fluvial valleys is one of the mass movement types that have caused the largest number of casualties in Spain (Guerrero *et al.*, 2004a; Gutiérrez *et al.*, 2008a). Four rock-fall events from a gypsum cliff occurred in 1856, 1874, 1903 and 1946 and killed a total of 106 people in Azagra village, situated in the Ebro Valley upstream of the study area (Ayala *et al.*, 1998). A rock-fall from the gypsum escarpment that flanks the Jalón River valley in Calatayud caused the loss of one life in 1988 (Gutiérrez and Cooper, 2002).

In the investigated sector, the Quaternary terrace, pediment and valley fill deposits show some peculiar characteristics related to the highly soluble nature of the halite- and glauberite-bearing evaporitic bedrock (Gutiérrez *et al.*, 2008a): (1) The Quaternary alluvium shows dramatic thickness changes locally reaching as much as 100 m. These thickened deposits fill basins and troughs up to 30 km long generated by synsedimentary subsidence caused by the karstification of the soluble bedrock (Benito *et al.*, 1998). A recent investigation by Guerrero *et al.* (2008a) in the Huerva River valley reveals that this large-scale subsidence phenomenon coeval to fluvial aggradation is primarily related to the interstratal dissolution of halite units. (2) The Quaternary cover, and very frequently the underlying evaporitic bedrock, show abundant gravitational deformation caused by dissolution of the substratum at the alluvium-bedrock boundary (rockhead karstification) and within the evaporitic succession (interstratal karstification) (Guerrero *et al.*, 2004b, 2008a and b). Three main subsidence mechanisms have been identified in these subsidence structures, which constitute the geological record of past sinkhole activity (Gutiérrez *et al.*, 2008a, c); sagging (progressive downward flexure), suffosion (downward migration of detrital particles through karst conduits) and collapse (brittle deformation by brecciation and/or through the development of discrete failure planes).

(Figure 2)

3. The Sinkhole Hazard and Risk in the Ebro Valley

The presence of Quaternary deposits and the relative height of the alluvial surfaces above the river channel (relative age) constitute major controls in the spatial distribution of sinkholes in the analyzed stretch of the Ebro River valley. Most of the sinkholes occur in areas where the bedrock is covered by Quaternary alluvial deposits (mantled karst); evidence of subsidence activity is very scarce in the gypsum outcrops (bare karst) (Gutiérrez and Gutiérrez, 1998). Additionally, the highest densities and probabilities of occurrence of sinkholes are associated with the floodplains and the lower terraces. This general spatial distribution pattern can be attributed to two main circumstances: (1) The Quaternary fluvial deposits behave as discharge zones for the underlying karstic aquifer when situated at the valley bottom (floodplain), and become recharge areas dominated by downward vadose flows where they are transformed into perched aquifers (terraces) as a consequence of fluvial entrenchment. (2) Most of the human activity, including irrigation and groundwater pumping, is concentrated in the floodplain and the lower alluvial levels.

The convergence in the lower terraces of a high sinkhole activity (hazard) and the presence of abundant vulnerable human structures and economic activities (exposure) results in high risk situations. The Ebro valley in the outskirts of Zaragoza is the area in Europe where the subsidence risk due to evaporite dissolution has the greatest economic impact (Gutiérrez *et al.*, 2008a). A relevant factor is that collapse sinkholes that occur in a catastrophic way might result in the loss of human lives as it has been documented in other karst areas (e.g. De Bruyn and Bell, 2001). Some examples illustrate the significance of the detrimental effects caused by sinkholes on the economic development of the area: (1) The construction of the Imperial Canal, which runs along the southern margin of the Ebro valley, was stopped in 1790 downstream of Zaragoza, 50 km short of its intended length due to continuous failures caused by sinkholes (Sástago, 1796; Gutiérrez *et al.*, 2007); (2) In the Gállego River valley, the totality of Puilatos village was demolished in 1985 due to structural damage caused by dissolution-induced subsidence; (3) Numerous buildings and factories built on artificially filled active sinkholes have been demolished (Galve *et al.*, 2009). At the present time, the rapid tilt that affects a recently built building with 100 flats, partially constructed on a well-known sinkhole, might result in unacceptable structural damage (Gutiérrez *et al.*, 2009)

Another relevant aspect for this investigation is the distribution of the different types of sinkholes and their activity. Following the genetic classification proposed by

Gutiérrez *et al.* (2008c), three main types of sinkholes may be differentiated in the study area: (a) Cover collapse sinkholes formed by downward migration of cover deposits through dissolutional conduits. These are holes with scarped edges typically less than 2 m across. This type of sinkholes, frequently induced by sheet-flood irrigation, reaches minimum probabilities of occurrence of 45 sinkholes/km^2/y in the lower terraces downstream of Zaragoza (Gutiérrez *et al.*, 2007). A priori, the InSAR technique is not appropriate for detecting the ground subsidence produced by these sinkholes because of their small size and the loss of correlation produced in the rapidly sinking land surface. (b) Cover and bedrock collapse sinkholes, commonly more than 10 m in diameter and generated by upward stoping of large cavities formed within the evaporitic bedrock. A density of 600 sinkholes/km^2/y and a percentage of sinkhole area of around 20% have been documented in a small field of cover and bedrock collapse sinkholes close to La Puebla de Alfindén village (Gutiérrez-Santolalla *et al.*, 2005a). (c) Cover and bedrock sagging sinkholes resulting from passive sagging of the alluvial mantle and underlying bedrock caused by interstratal karstification. This type of sinkholes, usually more than 100 m in length, has been mapped in the floodplain upstream and downstream of Zaragoza and in the lower terraces upstream of Zaragoza (Gutiérrez *et al.*, 2007; Galve *et al.*, 2009). In practice, numerous sinkholes result from the combination of sagging and collapse mechanisms. Type b sinkholes may undergo both gradual and catastrophic subsidence, whereas type c sinkholes are characterized by gradual deformation. The majority of the type b and c sinkholes identifiable in aerial photographs from 1956 are now filled by man-made ground and a significant proportion of them have been used for urbanization (Soriano and Simón, 1995; Galve *et al.*, 2009). This is the reason why most of the subsidence damage in the area is not related to the occurrence of new sinkholes, but to the activity of previously existing ones (Gutiérrez *et al.*, 2008a, 2009; Galve *et al.*, 2009).

4. Materials and Methodology

4.1. SAR Imagery

The large archive of ERS-1 and ERS-2 images acquired since 1992 was examined. These images were acquired with a 35-day repeat period at a regular nominal incidence angle of 23º and with a frequency band of 5.33 GHz (5.65 cm wavelength). From the 200 archived images covering the study area we selected a series of 27 ERS-1 and ERS-2 images (Table 1) acquired on descending orbits (track 237, frame 2766). The available number of ascending SAR ERS images was smaller (track 330, frame 837) and they were not uniformly distributed in the different years (track 58, frame 837).

The selected images span more than five years, from 5 July 1995 to 21 December 2000, with a uniform distribution in the different seasons. Images acquired later than 2000 were discarded because of the significant degradation in Doppler centroid stability of ERS-2 (Miranda *et al.*, 2005).

(Table 1)

4.2. SBAS-DInSAR Technique

The Small BAseline Subset (SBAS) technique is based on the combination of DInSAR interferograms computed from a set of SAR images obtained at different dates. A key step in this approach is the adequate selection of the appropriate SAR image pairs for generating the interferograms. Image pairs are selected to minimise noise effects referred to as decorrelation phenomena (Zebker and Villasenor, 1992) in order to maximize the number of coherent pixels. Selection of valid image pairs is accomplished by limiting the maximum spatial and temporal separation (“baseline”) between the orbits of the interferometric SAR image pairs, and the frequency shift between the Doppler centroids (Franceschetti and Lanari, 1999). The SBAS-DInSAR technique allows generating spatially dense mean deformation velocity maps and displacement time-series. In this section, the key issues of the technique are presented. A detailed analysis of the algorithm can be found in Berardino et al. (2002).

The raw SAR data were focused and co-registered with respect to a common (reference) acquisition geometry (ERS-2 image acquired on 5 February 1998). Only those interferometric SAR image pairs with a maximum spatial separation (baseline) between the orbits of 300 m and a maximum time span of 1400 days were selected. Based on such constraints 74 interferograms were generated at low spatial resolution (multilook interferograms). Coherence and intensity images created for all the 74 combinations (interferograms) were used to improve the unwrapping process. Only those pixels with a coherence >0.75 were kept for phase information analysis.

The topographic phase was removed by using the Shuttle Radar Topography Mission (SRTM) DEM, with a 90-m pixel size and an absolute vertical accuracy greater than 16 m (Farr *et al.*, 2007). Moreover, the precise orbit state vectors (time, velocity and position) calculated by Delft University for ERS satellites (*Scharroo and Visser*, 1998) were used to reduce orbital errors.

The phase information of each multilook interferogram was unwrapped by applying the extended minimum cost flow algorithm described by Pepe and Lanari (2006). A region growing procedure was used to get better performances in areas with low signal to noise ratio. A reference point located in Zaragoza city was selected as a stable reference SAR pixel to calibrate each interferogram. We chose this point because in this sector of the city, underlain by indurated alluvium more than 50 m thick, there is no identifiable evidence of recent deformation.

The deformation time series were retrieved for each coherent pixel by exploiting the Singular Value Decomposition method (Berardino *et al.,* 2002) which allowed us to "link" the unwrapped phase of DInSAR interferograms separated by large temporal and spatial baselines.

In order to avoid the atmospheric noise produced by heterogeneities between the radar acquisitions, the deformation estimates were filtered using the space-time DInSAR phase information. The filtering was implemented by exploiting the high correlation in space but poor in time of the atmospheric phase component. The atmospheric artifacts were identified via the cascade of a low-pass filtering, carried out in the two-dimensional spatial domain, followed by a temporal high-pass filtering. This process also allowed detecting possible orbital ramps caused by inaccuracies in the SAR sensors orbit information. Following their identification, the atmospheric artifacts and the orbital ramps were removed. Finally, deformation time-series related to the observed time period were produced in a spatially dense area. Results were given at a ground resolution of about 90 m × 90 m.

5. Results

A mean deformation velocity map (Figure 3) of the study area for the period 1995-2000 has been obtained applying the SBAS approach to the selected interferograms. The velocity estimates represent the displacement of the ground surface projected onto the satellite line of sight (LOS) and relative to the zero deformation reference point. Negative and positive values indicate subsidence and uplift, respectively.

The deformation map provides reliable information over a relatively large area, characterized by a high coherent (>0.75) region in terms of C-band radar echoes. The computed deformation velocity ranged from 1.65 cm/y of subsidence to 0.99 cm/y of uplift. The areas with absolute deformation velocity lower than 0.2 cm/y can be considered as stable or affected by displacement rates less than the accuracy of the method.

The detection of deformation areas was largely limited by the land covers. The outcrops of the Zaragoza Gypsum Formation largely covered with sparse xerophytic vegetation (around 10% of the area) preserved coherence between the dates of the radar images due to the low coverage, small size, and slow growth of the vegetation. A significant proportion of the identified deformation areas occur in urbanized and developed areas (2% of the study area) where pavements and human structures provide stable scattering surfaces that favor the persistence of the coherence. Conversely, in agricultural areas (more than 60% of the study area) the coherence and consequently the displacement measurement degrade. This is especially evident in the floodplains and lower terraces devoted to irrigated agriculture. The frequent changes in geometry and moisture due to variations in the phenological state of the crops, agricultural practices, and frequent wind, produce a loss of correlation in the radar signal. In the dry farmed fields devoted to winter cereal the coherence was locally preserved.

At a local scale the map delineates several deformation zones in the Ebro River valley (Figure 3). Two subsidence sites correspond to developed areas located on the lowest terrace and floodplain of the Ebro River and underlain by known active sinkholes (sites 1 and 2). Three deformation sites are located in gypsum outcrops covered with sparse xerophytic vegetation. Two of them (sites 3 and 4) are related to active landslides located in the gypsum escarpment and the other one (site 5) provides the first account of subsidence over a salt mine under exploitation.

The deformation sites identified by the SBAS DInSAR technique were analyzed through the elaboration of detailed geomorphological maps combining aerial photograph interpretation and field surveys. The temporal evolution of the deformation and the available rainfall and discharge records have been compared in order to elucidate whether they exhibit some mutual correlation. The data obtained by means of traditional geomorphological studies concerning sinkhole and landslide distribution and activity have allowed us to assess qualitatively the advantages and limitations of the SBAS DInSAR technique in the area.

(Figure 3)

5.1. Sinkholes

The extensive geomorphological investigations carried out in the Ebro River valley reveal that active subsidence associated with sinkholes affects a significant proportion of the floodplain and lower terraces (e.g. Soriano and Simón, 1995; Gutiérrez *et al.*, 2007; Galve *et al.*, 2009). However, our DInSAR analysis has missed most of the known areas where there is evidence of dissolution-induced ground settlement. The deformation caused by the numerous cover collapse sinkholes that form in the lower terrace of the Ebro valley downstream of Zaragoza city (>45 sinkholes/km^2/y; Gutiérrez *et al.*, 2007) has not been detected due to the following reasons: (1) These sinkholes form in a sudden way and their size, commonly 1.5-2 m in diameter, is much less than that of the radar resolution cell (90 m × 90 m); (2) Most of them occur in cultivated fields irrigated by sheet-flooding (Gutiérrez *et al.*, 2007), producing temporal decorrelation.

The DInSAR map provides deformation measurements in a small proportion of the abundant large sinkholes (cover and bedrock sagging sinkholes and cover and bedrock collapse sinkholes) in which active subsidence has been documented. For example, in a sector of the valley (40.8 km^2) upstream of Zaragoza city, large cover and bedrock sagging sinkholes cover approximately 8% of the area and more than 20% of them show evidence of ground deformation. In the same area, at least 58% of the cover and bedrock collapse sinkholes are active (Galve *et al.*, 2009). Most of the subsidence areas detected by the SBAS DInSAR technique occur associated with human structures built on artificially filled sinkholes. These sinkholes are clearly identifiable in old aerial photographs and topographic maps and the buildings and roads constructed on them display conspicuous deformations. Several factors may have limited the capability of the applied approach to detect displacement: (1) A large percentage of these depressions occur in agricultural land and some are frequently filled by artificial deposits; (2) A smaller pixel size may be required to detect deformation in some active sinkholes; (3) The subsidence rate of some sinkholes may be either too high or too low for its detection by the ERS SAR system; (4) A shallow water table, especially in those depressions located in the floodplain, cause flooding and changes in the soil moisture probably leads to a loss of coherence.

The DInSAR analysis has provided consistent subsidence measurements in two areas located in the lower terrace and floodplain of the Ebro valley upstream (site 1) and downstream (site 2) of Zaragoza city (Figures 1 and 3). In site 1 (Figure 4), all of the subsidence points occur associated with previously mapped sinkholes (Galve *et al.*, 2009). A cluster of deformation points coincides with a sinkhole formerly hosted a swampy area (Galve *et al.*, 2009). This depression was covered with man-made ground and devoted to the construction of the El Portazgo Industrial State (Figure 4). Here, numerous factories and warehouses have been demolished and most of the existing buildings show evident signs of settlement (Figure 4D). Additionally, in this sector the N-232 highway is locally affected by progressive subsidence at rates of the order of cm/y. Most likely the road resurfacing repairs carried out on a yearly basis precludes the detection of the deformation by means of the DInSAR technique.

In site 1 the subsidence rates provided by the DInSAR range from 0.25 to 1.68 cm/y (Figure 4C). The area represented by the pixel with the highest subsidence rate (1.68 cm/y) includes a collapse sinkhole about 15 m in diameter that formed suddenly in 1994 in the interior of a warehouse (Galve *et al.*, 2009). These values are in agreement with subsidence rates of 3.2-4 cm/y measured by leveling at some of the most active points in El Portazgo Industrial State (Simón *et al.*, 2008). The temporal evolution pattern of the subsidence is illustrated in Figure 5, in which the selected measurement point reflects the progressive deformation recorded in the area. The high subsidence rates may be related to the contribution of both dissolution of salt-bearing evaporites and compaction-consolidation of anthropogenic and sinkhole fill deposits (Galve *et al.*, 2009; Gutiérrez *et al.*, 2009).

(Figure 4)

(Figure 5)

The deformation area detected at site 2 (Figure 6) coincides with a cover and bedrock collapse sinkhole about 300 m long and 4 m deep (Gutiérrez-Santolalla *et al.*, 2005b). The aerial photograph taken in 1956 shows a large funnel-shaped depression with a nested collapse sinkhole with fresh bedrock scarps (Figure 6B). This depression, locally known as "Las Rajas" (meaning "the cracks"), was originally used as an illegal waste disposal site. Subsequently, it was covered by artificial fill and used for the construction of two blocks of the Malpica Industrial State. These two blocks are the only structures of the industrial state that show any evidence of subsidence deformation. A grouting program was carried out in 2006 to arrest the subsidence process. The mean subsidence rates measured in this sinkhole range from 0.32 to 0.43 cm/y and the maximum cumulative displacement reaches 2.45 cm. Here, subsidence may be related to both karstic collapse and compaction of loosely packed artificial deposits.

(Figure 6)

The subsidence rates measured in sites 1 and 2 do not show any significant correlation with the mean daily rainfall calculated for the time intervals defined by the radar dates. This is most likely related to the fact that the sinkholes in those sites result from deep-seated interstratal karstification and not from suffosion processes controlled by downward vadose flows. Additionally, the deformation time series from sinkhole sites show an anomalous slight uplift in 1997 (Figure 5). The record of the Zaragoza Airport weather station (WMO 08160) (Figure 1) indicates that 1997 was an exceptionally wet year in the last decades, with an annual total of 480 mm, being the average 311 mm. This uplift period coincides with high values of mean daily rainfall (Figure 5) and with the maximum number of significant rainfall events (>20 mm) over the periods studied. We are not able to provide a satisfactory physical explanation for such a phenomenon affecting a built-up area, which could correspond to an artifact. Further research including ground leveling could shed light on this issue.

5.2. Landslides

The DInSAR has detected ground motion in a small proportion of the numerous active landslides that affect the stretch of the gypsum escarpment situated upstream of Zaragoza city (Figures 1, 3 and 7). The deformation points in this segment of the scarp are concentrated around Las Torres stream (site 3). Downstream of Zaragoza city, the DInSAR has provided deformation measurements for the only landslide previously mapped as active (Gutiérrez *et al.*, 1994; site 4; Figure 2A). Some of the factors that may have determined the limited capability of the technique to detect ground displacement in active landslides include: (1) The vertical and lateral displacement rates in some landslides may be outside of the measurement range of the method; (2) The pixel size may be too large to obtain measurements in some landslides; (3) The parallelism between the NW-SE-trending escarpment and the ERS satellite line of sight limit the capability of the method because the landslides moving perpendicular to the escarpment are moving in the geometrically least favorable direction for the ERS satellite to resolve this motion with respect to its line of sight. The use of both ascending and descending tracks may help to partially overcome this problem.

.

(Figure 7)

In site 3 all of the deformation points occur associated with active landslides, some of which interact with and partially invade the present channel of the Ebro River (Figure 7). Here, the average deformation ranges from 0.22 to 0.80 cm/y. In site 4 the mean displacement varies from 0.27 to 0.46 cm/y. The deformation time series in both areas show a linear trend interrupted by sporadic and asynchronous episodes of apparent uplift (Figure 8). This uplift could be interpreted as: (1) The expected local upward displacement in rotational landslides; (2) Expansion of the soil due to increased rainfall-derived moisture. Vertical movements in clay soils resulting from variations in water content can reach several cm (Marshall *et al.*, 1996). This kind of deformation has been detected by means of radar interferometry (Gabriel *et al.*, 1996). To our knowledge, there is no study dealing with similar deformations in gypseous soils, although slickensides indicative of vertical relative displacements of blocks in gypseous soils horizons have been reported by Herrero *et al*. (2009, accepted). Moreover, an additional effect related to the wetting-drying cycles affecting the biological crust in these soils can also be invoked. In fact, there is a relatively good correlation between the uplift periods and relatively humid time intervals as defined by the mean daily rainfall values estimated from the precipitation record of Remolinos weather station (9338A) (Figure 8), located near site 3 (Figure 1). The highest values of mean daily rainfall and the highest number of significant rainfall events coincides with 1997 and 1999 uplift episodes.

There is also a lack of synchronicity in the motion among the different points that can be related to the expected variable kinematics of the slope movements. Additionally, no correlation has been found between the high and low discharge events in the Ebro River and the temporal evolution of the deformation over the analyzed period in the landslides associated with the river channel. This lack of correlation is probably due to the fact that no severe flood events occurred during that period; all of the peak discharge values are attributable to return periods less than 10 years.

(Figure 8)

5.3. Mining Subsidence in Remolinos

An halite unit situated about 70-75 m above the Ebro River channel has been mined in the Remolinos area since Roman times (Figures 1, 3). Most of the salt extraction has been concentrated in two mines: Mina Real and María del Carmen, located in Las Salinas and El Agua streams, respectively (Figure 9). In Mina Real, inactive since 1989, the salt was excavated by the longwall method with galleries and pillars 18 and 20-25 m wide, respectively. At the present time halite is extracted by the room and pillar method from María del Carmen mine, with an annual production of around 600,000 Tn. In this mine the rooms and pillars are 20 m wide and 5.6-5.8 m high and the excavation fronts advance at an average annual rate of around 40 m (Iberica de Sales S.A., pers. comm.).

In this area the sparse xerophytic vegetation covering the gypsum outcrops gives rise to good coherence of C-band and thus the detection of phase differences. The DInSAR map delineates two deformation zones located along the Las Salinas stream and in the El Agua catchment and adjacent areas (Figure 9). Active landslides are abundant due to the following factors: (1) The rapid entrenchment of the drainage network induced by the local base level drop resulting from the retreat of the Ebro River escarpment; (2) The presence of landslide-prone shale units and halite sediments affected by interstratal karstification. The shale units control the development of rotational and lateral spreading movements.

In order to elucidate the role played by the slope movements and mining subsidence in the deformation detected in the two areas, a landslide map has been produced by means of aerial photograph interpretation and field surveys (Figure 9B). In Las Salinas stream area all of the deformation points fall on the upper part of active landslides and away from the excavations of Mina Real mine. The crown sector of these landslides shows conspicuous fresh scars, scarps and unloading cracks (Figure 9C). The displacement velocity in this area ranges from 0.24 to 1.45 cm/y. Conversely, all of the deformation points in El Agua stream catchment area, except the one associated with the entrance of the María del Carmen mine, occur on slopes devoid of landslides and underlain by the mine openings (Figure 9). The entrance of María del Carmen mine is located in a rotational landslide. On 7 July 2004, the undermined landslide mass suddenly collapsed trapping a truck (Figure 9D). Fortunately, the driver got out unscathed. Possibly, the displacement detected by the DInSAR (0.27 cm/y) records a premonitory creep deformation that preceded the catastrophic movement. The mining subsidence detected in the rest of the points reaches a maximum displacement rate of 1.45 cm/y. The graphs that represent cumulative deformation versus time for these points reveal a progressive subsidence punctuated by episodes of a subtle apparent uplift (Figure 10). These uplift episodes, that show a good correlation with humid periods, might be related to volume changes in the soil related to the variable moisture content. Detailed field measurements would be necessary to test this hypothesis.

(Figure 9)

(Figure 10)

6. Discussion and Conclusions

The SBAS DInSAR analysis has been applied in an evaporitic area whose geomorphology has been profusely studied in previous works. The capability of the SBAS technique to detect ground displacement has been tested using an ERS data set including 27 images covering more than five years (1995-2000). The obtained results delineate deformation zones providing values of displacement (magnitude and rate). The detected zones affected by ground motion coincide with known active sinkholes and landslides and with the area underlain by an active salt mine. The obtained DInSAR deformation map provides the first account of mining subsidence in the area. The measured deformation rates reach 1.68 cm/y for the sinkholes, 0.80 cm/y for the landslides and 1.45 cm/y for the area affected by mining subsidence. The temporal deformation series reveal a progressive downward displacement associated with the three phenomena over the analyzed time span. This displacement does not show a clear relationship with rainfall and the maximum determination coefficient ($r^2 < 8$) corresponds to the cumulative rainfall of the previous week for landslide and mining areas, and to the monthly rainfall for the sinkhole area. The apparent uplift episodes measured by the DInSAR in 1997 and 1999, which seem to correlate with more humid periods, might be related to volume changes in the gypseous soil horizons controlled by changes in the water content. Detailed field measurements would be necessary to check this hypothesis.

The SBAS DInSAR analysis has provided deformation measurements in a small proportion of the known active sinkholes and landslides due to the following reasons: (1) The lack of coherence in agricultural areas; the majority of the active sinkholes occur in the floodplain and lower terraces largely devoted to irrigated crops. Most of the deformation points related to dissolution-induced subsidence occur in developed areas underlain by artificially filled sinkholes (2) The pixel size of 90 m x 90 m was too large to detect small landslides and sinkholes, particularly small cover collapse sinkholes. (3) The ground motion in some sinkholes and landslides may be too slow or too fast to be measured using the DInSAR method used here. (4) The parallelism between the NW-SE-trending escarpment and the ERS satellite line of sight makes difficult the acquisition of deformation measurements. The displacements in a direction perpendicular to the line of sight are the least favorable to be measured.

Although the DInSAR results have missed a significant proportion of the active sinkholes and landslides identified by traditional geomorphological methods (mainly aerial photographs and field surveys), it provides valuable supplementary data including: (1) Areas affected by mining subsidence which could only be recognized by geodetic methods; (2) Measurements of deformation magnitude and rate; (3) Creep deformation in landslides and sinkholes which might correspond to premonitory indicators of catastrophic mass movements, as seems to have been the case of the rapid landslide that occurred at the entrance of María del Carmen salt mine. Another important advantage of the SBAS DInSAR method is that it allows analyzing large areas even in non accessible or remote zones. Consequently, a good option is to complement both geodetic and InSAR methods like with traditional geomorphological studies.

The principal limitations of the obtained DInSAR results include: (1) Lack of measurements in a large proportion of the study area due to temporal decorrelation or incoherence largely controlled by the land covers. (2) Limited spatial resolution caused by the large pixel size in the deformation map. (3) Unsuitability to detect catastrophic collapse sinkholes and landslides. (4) Limited temporal length of the measurements. These limitations can be partially overcome by conducting more detailed DInSAR analysis of specific sites using SAR images of different wave-lengths (L band and X band) and a higher resolution DEM in combination with other methods including: geomorphological mapping, high-resolution ground-based geodetic surveys, retrodeformation analysis and dating of recent deposits affected by displacement. Additionally, it would be interesting to test whether those detailed analysis could allow detecting precursor indicators of catastrophic deformation events in linear infrastructures like the highly vulnerable high-speed Madrid-Zaragoza-Barcelona railway (Guerrero *et al.*, 2008b).

Acknowledgements

This work was carried out as part of the projects AGL2006-01283 (Spanish Ministry of Science and Education), PM008/2007 (Aragón Government) and CGL2007-60766 (FEDER and Spanish Ministry of Science and Education). The authors would like thank to the European Space Agency for providing the ERS images under the Project ID C1P-3462 and to Iberica de Sales S.A for providing information on the salt mining operations in the Remolinos area.

References

Amelung F, Galloway DL, Bell JW, Zebker HA, Laczniak RJ. 1999. Sensing the ups and downs of Las Vegas: InSAR reveals structural control of land subsidence and aquifer-system deformation. *Geology* **27**: 483-486.

Arlegui L, Simón JL. 2001. Geometry and distribution of regional joint sets in a non-homogeneneous stress field: case study in the Ebro Basin (Spain). *J. Struct. Geol*. **23**: 297-313.

Ayala F, Aparicio V, Conconi G. 1988. Estudio de inestabilidades en los acantilados yesíferos de la ribera de Navarra. II Simposio sobre taludes y laderas inestables. Andorra, 657-668.

Benito G, Pérez-González A, Gutiérrez F, Machado MJ. 1998. River response to Quaternary subsidence due to evaporite solution (Gállego River, Ebro Basin, Spain). *Geomorphology* **22**: 243-263.

Baer G, Schattner U, Wachs D, Sandwell D, Wdonwinski S, Frydman S. 2002. The lowest place on Earth is subsiding —An InSAR (Interferometric Synthetic Aperture Radar) perspective. *Geol. Soc. Am. Bull.* **114**: 12-23.

Berardino P, Fornaro G, Lanari R, Sansoti E. 2002. A new algorithm for surface deformation monitoring based on Small Baseline Differential SAR Interferograms. *IEEE Trans. Geosci. Remote Sens*. **40**: 2375-2383.

Berardino P, Casu F, Fornaro G, Lanari R, Manunta M, Manzo M, Sansosti E. 2004. A quantitative analysis of the SBAS algorithm performance. International Geoscience and Remote Sensing Symposium (IGARSS 2004) **5**: 3321-3324.

Berardino P, Casu F, Manunta M, Manzo M, Pepe A, Pape S, Sansoti E, Solaro G, Tizzani P, Zeni G, Lanari R. 2007. The Sbas.DInSAR approach for surface deformation analysis of active volcanic areas. *Geophys. Res. Lett.* **9**: 03724.

Borgia A, Tizzani P, Solaro G, Manzo M, Casu F, Luongo G, Pepe A, Berardino P, Fornaro G, Sansosti E, Ricciardi GP, Fusi N, Di Donna G, Lanari R. 2005. Volcanic spreading of Vesuvius, a new paradigm for interpreting its volcanic activity. *Geophys. Res. Lett.* **32**: 1-4.

Bovenga F, Nutricato R, Refice A, Wasowski J. 2006. Application of Multitemporal Differential Interferometry Analysis for Detecting Slope Instability in Urban/Peri-Urban Areas. *Eng. Geol*. **88**: 218-239.

Burbank DW, Anderson RS 2001. Tectonic Geomorphology. Blackwell Science Ltd. Oxford, United Kingdom, 274 p.

Cascini L, Ferlisi S, Fornaro G, Lanari R, Peduto D, Zeni G. 2006. Subsidence monitoring in Sarno urban area via multi-temporal DInSAR technique. *Int. J. Remote Sens.* **27**: 1709-1716.

Casu F, Manzo M, Lanari R. 2006. A quantitative assessment of the SBAS algorithm performance for surface deformation retrieval from DInSAR data. *Remote Sens. Environ.* **102**: 195-210.

Casu F, Manzo M, Lanari R. 2008. SBAS-DInSAR Analysis of Very Extended Areas: First Results on a 60,000 km^2 Test Site. *IEEE Geosci. Remote Sens. Lett.* **5:** 3. DOI:10.1109/LGRS.2008.916199.

Cavalié O, Doin MP, Laserre C, Briole P. 2007. Ground motion measurement in the Lake Mead area, Nevada, by differential synthetic aperture radar interferometry time series analysis: probing the lithosphere rheological structure. *J. Geophys. Res.* **11**: B03403.

Closson D, Karaki NA, Klinger Y, Hussein MJ. 2005. Subsidence and sinkhole hazard assessment in the Southern Dead Sea area, Jordan. *Pure Appl. Geophys.* **162**: 221-248.

Colesanti C, Wasowski J. 2006. Investigating landslides with space-borne synthetic aperture radar (SAR) interferometry. *Eng. Geol.* **88**: 173-199.

Crosetto M, Castillo M, Arbiol R. 2003. Urban subsidence monitoring using radar interferometry: Algorithms and validation. *Photogramm. Eng. Rem. Sen.* **69**: 775-783.

Crosetto M, Crippa B, Biescas E. 2005. Early detection and in-depth analysis of deformation phenomena by radar interferometry. *Eng. Geol.* **79**: 81-91.

De Bruyn IA, Bell FG. 2001. The occurrence of sinkholes and subsidence depressions in the Far West Rand and Gauteng Province, South Africa, and their engineering implications. *Environ. Eng. Geosci.* **7**: 281-295.

Farr TG, Rosen PA, Caro E, Crippen R, Duren R, Hensley S, Kobrick M, Paller M, Rodríguez E, Roth., Seal D, Shaffer S, Shimada J, Umland J, Werner M, Oskin M, Burbank D, Alsdorf D. 2007. The shuttle radar topography mission. *Rev. Geophys.* **45**.

Fernández J, Yu TT, Rodríguez-Velasco J, González-Matensanz J, Romero R, Rodríguez G, Quirós R, Dalda A, Aparicio A, Blanco MJ. 2003. New geodetic monitoring system in the volcanic island of Tenerife, Canaries, Spain. Combination of InSAR and GPS techniques. *J. Volcanol. Geoth. Res.* **124**: 241-253.

Ferretti A, Prati C, Rocca F. 2000. Non-linear Subsidence Rate Estimation Using Permanent Scatterers in Differential SAR Interferometry. *IEEE Trans. Geosci. Remote Sens*. **38**: 2202-2212.

Ferretti A, Prati C, Rocca F. 2001. Permanent Scatteres in SAR interferometry. *IEEE Trans. Geosci. Remote Sens.* **39**: 8-20.

Ferretti A, Marco B, Fabrizio N, Claudio P. 2004. Possible utilizzo di dati radar satellitari per individuazione e manotiraggio di fenomini di sinkholes. In: Nisio, S.; Panetta, S. and Vita, L. (Eds.). Stato dell'arte sullo studio dei fenomeni di sinkholes e ruolo delle amministrazioni statali e locali nel governo del territorio, APAT, Roma, 331-340.

Fialko Y, Sandwell D, Simons M, Rosen P. 2005. Three-dimensional deformation caused by the Bam, Iran, earthquake and the origin of shallow slip deficit. *Nature* **435**: 295-299.

Franceschetti G, Lanari R. 1999. Synthetic Aperture Radar processing. CRC Press, Boca Raton, Florida.

Gabriel AK, Goldstein RM, Zebker HA. 1989. Mapping small elevation changes over large areas: differential radar interferometry. *J. Geophys. Res.* **94**: 9183-9191.

Galloway DL, Hudnut KW, Ingebritsen SE, Phillips SP, Peltzer G, Rogez F, Rosen PA. (1998). Detection of aquifer system compaction and land subsidence using interferometric synthetic aperture radar, Antelope Valley, Mojave Desert, California, *Water Resour. Res.* **34**: 2573-2585.

Galloway DL, Jones DR, Ingebritsen SE. 1999. Land subsidence in the United States: U.S. Geological Survey Circular 1182, 175p.

Galve JP, Gutiérrez F, Lucha P, Bonachea J, Cendrero A, Gimeno MJ, Gutiérrez M, Pardo G, Remondo J, Sánchez JA. 2009. Sinkholes in the salt-bearing evaporite karst of the Ebro River valley upstream of Zaragoza city (NE Spain).

Geomorphological mapping and analysis as a basis for risk management, *Geomorphology*, in press.

García-Castellanos D, Vergés J, Gaspar-Escribano J, Cloetingh S. 2003. Interplay between tectonics, climate and fluvial transport during the Cenozoic evolution of the Ebro Basin (NE Iberia). *J. Geophys. Res.* **108**: 2347, ETG 8-1/8-18.

Ge L, Chang H-C, Ng AH, Rizos C. 2007. Radar Interferometry for safe coal mining in China. *Photogramm. Eng. Rem. Sen.* **73**: 259-266.

Goldstein RM, Engelhardt H, Kamb B, Frolich RM. 1993. Satellite radar interferometry for monitoring ice-sheet motion - Application to an Antarctic ice stream. *Science* **262**: 1525-1530.

Guerrero J. 2008. Dinámica fluvial y riesgos naturales derivados de la subsidencia kárstica en los valles del Huerva y del Ebro. University of Zaragoza. PhD Thesis, 348 p.

Guerrero J, Gutiérrez F, Lucha P. 2004a. El riesgo de movimientos de ladera en escarpes yesíferos. El caso de la localidad de Cadrete (Depresión del Ebro). In: Benito, G. and Díez Herrero, A. (Eds.). Riesgos Naturales y Antrópicos en Geomorfología. VIII Reunión Nacional de Geomorfología. Sociedad Española de Geomorfología. Toledo, 453-461.

Guerrero J, Gutiérrez F, Lucha P. 2004b. Paleosubsidence and active subsidence due to evaporite dissolution in the Zaragoza city area (Huerva River valley, NE Spain). Processes, spatial distribution and protection measures for linear infrastructures. *Eng. Geol.* **72**: 309-329.

Guerrero J, Gutiérrez F, Lucha P. 2008a. The impact of halite dissolution subsidence on fluvial terrace development. The case study of the Huerva River in the Ebro Basin (NE Spain).*Geomorphology* **100**: 164-179

Guerrero J, Gutiérrez F, Bonachea J, Lucha P. 2008b. A sinkhole susceptibility zonation based on paleokarst analysis along a stretch of the Madrid-Barcelona high-speed railway built over gypsum- and salt-bearing evaporites (NE Spain). *Eng. Geol.* **102**: 62-73.

Gutiérrez F, Cooper AH. 2002. Evaporite dissolution subsidence in the historical city of Calatayud, Spain: damage appraisal and prevention. *Nat. Hazards* **25**: 259-288.

Gutiérrez F, Arauzo T, Desir G. 1994. Deslizamientos en el escarpe de Alfajarín (Zaragoza). *Cuaternario y Geomorfología* **8**: 57-68.

Gutiérrez-Santolalla F, Gutiérrez-Elorza M, Marín C, Desir G, Maldonado C. 2005a. Spatial distribution, morphometry and activity of La Puebla de Alfindén sinkhole field in the Ebro River valley (NE Spain) applied aspects for hazard zonation. *Environ. Geol.* **48**: 360-369.

Gutiérrez-Santolalla F, Gutiérrez-Elorza M, Marín C, Maldonado C, Younger PL. 2005b. Subsidence hazard avoidance based on geomorphological mapping. The case study of the Ebro River valley mantled karst (NE Spain). *Environ. Geol*. **48**: 370-383.

Gutiérrez F, Galve JP, Guerrero J, Lucha P, Cendrero A, Remondo J, Bonachea J, Gutiérrez M, Sánchez JA. 2007. The origin, typology, spatial distribution, and detrimental effects of the sinkholes developed in the alluvial evaporite karst of the Ebro River valley downstream Zaragoza city (NE Spain). *Earth Surf. Proc. Land.* **32**: 912-928.

Gutiérrez F, Calaforra JM, Cardona F, Ortí F, Durán JJ, Garay P. 2008a. Geological and environmental implications of evaportie karst in Spain. *Environ. Geol.* **53**: 951-965.

Gutiérrez F, Cooper AH, Johnson KS. 2008b. Identification, prediction and mitigation of sinkhole hazards in evaporite karst areas. *Environ. Geol.* **53**: 1007-1022.

Gutiérrez F, Guerrero J, Lucha P. 2008c. A genetic classification of sinkholes illustrated from evaporite paleokarst exposures in Spain. *Environ. Geol*. **53**: 993-1006.

Gutiérrez F, Ortuño M, Lucha P, Guerrero J, Acosta E, Coratza P, Piacentini D, Soldati M. 2008d. Late Quaternary episodic displacement on a sackung scarp in the central Spanish Pyrenees. Secondary paleoseismic evidence?, *Geodinámica Acta* **21**: 187-202.

Gutiérrez F, Galve JP, Lucha P, Bonachea J, Jordá L, Jordá R. 2009. Investigation of a large collapse sinkhole affecting a multi-storey building by means of geophysics and the trenching technique (Zaragoza city, NE Spain). *Environ. Geol*, in press.

Gutiérrez M, Gutiérrez F. 1998. Geomorphology of the Tertiary gypsum formations in the Ebro Depression (Spain). *Geoderma* **87**: 1-29.

Hansen H, Derauw D, Barcier C, Ozer A. 2003. Space-borne interferometric mapping of precursory deformation of a dyke collapse, Dead Sea area, Jordan. *Int. J. Remote Sens.* **24**: 843-849.

Hansen RF. 2001. Radar Interferometry: data interpretation and error analysis. Dordrecht: Kluwer Academic Publishers, Netherlands, 308 p.

Hanssen RF, Weckwerth TM, Zebker HA, Klees R. 1999. High-Resolution Water Vapour Mapping from Interferometric Radar Measurements. *Science* **283**: 1297-1299.

Herrera G, Tomas R, López-Sánchez JM, Delgado J, Mallorquí JJ, Duque S, Mulas J. 2007. Advanced DInSAR analysis on mining areas: La Unión case study (Murcia, SE Spain). *Eng. Geol*. **90**: 148-159.

Herrero J, Artieda O, Hudnall WH. 2009. Gypsum, a tricky material. *Soil Sci. Soc. Am. J.*, accepted.

Hoffman J, Zebker HA, Galloway DL, Amelung F. 2001. Seasonal subsidence and rebound in Las Vegas Valley, Nevada, observed by synthetic aperture radar interferometry. *Water Resour. Res.* **37**: 1551-1566.

Hooper A, Zebker H, Segall P, Kampes B. 2004. A new method for measuring deformation on volcanoes and other natural terrains using InSAR persistent scatterers. *Geophys. Res. Lett.* **31**: L23611, doi: 10.1029/2004GL021737.

Hooper A, Zebker H, Segall P, Kampes B. 2007. Persistent Scatterer InSAR for Crucial Deformation Analysis, with Application to Volcan Alcedo, Galapagos. *J. Geophys. Res.* **112**: B07407. DOI: 10.1029/2006JB004763.

Kampes B. 2005. Displacement Parameter Estimation using Permanent Scatterer Interferometry. PhD Thesis, DLR, Oberpfaffenhofen, Germany.

Lanari R, Casu F, Manzo M, Lundgren P. 2007. Application of the SBAS-DInSAR technique to fault creep: a case study of the Hayward fault, California. *Remote Sens. Environ.* **109**: 20-28.

Lanari R, Lundgren P, Manzo M, Casu F. 2004. Satellite radar interferometry time series analysis of surface deformation for Los Angeles, California. *Geophys. Res. Lett.* **3**: L23613.

Legresy B, Rignot E, Tabacco IE. 2000. Constraining ice dynamics at Dome C, Antartica, using remotely sensed measurements., *Geophys. Res. Lett.* **27**: 3493-3496.

Le Mouélic S, Raucoules D, Carnec C, King C. 2005. A least squares adjustment of multi-temporal InSAR data: Application to the ground deformation in Paris. *Photogramm. Eng. Rem. Sen.* **71**: 197-204.

Lundgren P, Casu F, Manzo M, Pepe A, Berardino P, Sansoti E, Lanari R. 2004. Gravity and magma induced spreading of Mount Etna volcano revealed by satellite radar interferometry. *Geophys. Res. Lett.* **31**: L04602.

Manzo M, Ricciardi GP, Casu F, Ventura G, Zeni G, Borgström S, Berardino P, Del Claudio C, Lanari R. 2006. Surface deformation analysis in the Ischia Island (Italy) based on spaceborne radar interferometry. *J. Volcanol. Geotherm. Res.* **151**: 399-416.

Marshall TJ, Holmes JW, Rose CW. 1996. Soil Physics, Third Edition, Cambridge University Press, 453 p.

Massonnet D, Feigl K. 1998. Radar Interferometry and its application to changes in the Earth's surface. *Rev. Geophys.* **36**: 441-494.

Massonnet D, Rossi M, Carmona C, Adragna F, Peltzer G, Feigl K, Rabaute T. 1993. The displacement field of the Landers earthquake mapped by radar interferometry. *Nature* **364**: 138-142.

Massonnet D, Briole P, Arnaud P. 2005. Deflation of Mount Etna by spaceborne radar interferometry. *Nature* **375**: 567-570.

McCalpin JP, Hart EW. 2002. Ridge-top spreading features and relationship to earthquakes, San Gabriel Mountain region, southern California. Parts A and B, National Earthquake Hazard Reduction Program, U.S. Geological Survey, Technical report, 44 + 51 p.

Miranda N, Rosich B, Santella C, Grion M. 2005. Review of the impact of ERS-2 piloting modes on the SAR Doppler stability. ESA SP-572. In Proceedings of the 2004 ENVISATand ERS Symposium, Salzburg, Austria.

Mora O, Mallorquí JJ, Broquetas A. 2003. Linear and nonlinear terrain deformation maps from a reduced set of interferometric SAR images. *IEEE Trans. Geosci. Remote Sens.* **41**: 2243-2253.

Moro M, Saroli M, Salvi S, Stramondo S, Doumaz F. 2007., The relationship between seismic deformation and deep-seated gravitational movements during the 1997 Umbria-Marche (Central Italy) earthquakes. *Geomorphology* **89**: 297-307.

Pagli C, Pedersen R, Sigmundsson F, Feigl KL. 2003. Triggered fault slip on June 17, 2000 on the Reykjanes Peninsula, SW-Iceland captured by radar interferometry. *Geophys. Res. Lett.* **30**: 1273.

Pardo G, Arenas A, González A, Luzón A, Muñoz A, Pérez A, Pérez-Rivarés FJ, Vázquez-Urbez M, Villena J. 2004. La Cuenca del Ebro. In: Vera, J.A. (Ed.). Geología de España, SEG-IGME, Madrid, 533-539.

Pellicer F, Echevarría MT, Ibáñez MJ. 1984. Procesos actuales en el escarpe de yesos de Remolinos. *Cuadernos de Investigación Geográfica* **10**: 159-168.

Pepe A, Lanari R. 2006. On the extension of the minimum cost flow algorithm for phase unwrapping of multitemporal differential SAR interferograms. *IEEE Trans. Geosci. Remote Sens.* **44:** 2374-2383.

Pérez-Rivarés F, Garcés M, Arenas C, Pardo G. 2002. Magnetocronología de la sucesión miocena de la Sierra de Alcubierre (Sector Central de la Cuenca del Ebro). *Revista de la Sociedad Geológica de España* **15**: 217-231.

Pérez-Rivarés F, Garcés M, Arenas C, Pardo G. 2004. Magnetostratigraphy of the Miocene continental deposits of the Montes de Castejón (central Ebro Basin, Spain): geochronological and paleoenvironmental implications. *Geologica Acta* **2**: 221-234.

Quirantes J. 1978. Estudio sedimentológico y estratigráfico del Terciario continental de los Monegros. Institución Fernando el Católico, CSIC, Zaragoza, 200 p.

Raucoules D, Le Mouelic S, Carnec C, Maisons C, King C. 2003a. Urban subsidence in the city of Prato (Italy) monitored by satellite radar interferometry. *Int. J. Remote Sens.* **24**: 891-897.

Raucoules D, Maisons C, Carnec C, Le Mouelic S, King C, Hosford S. 2003b. Monitoring of slow deformation by ERS radar interferometry on the Vauvert salt mine (France). Comparison with ground-based measurements. *Remote Sens. Environ.* **88**: 468-478.

Sarti F, Arkin Y, Chorowicz J, Karnieli A, Cunha T. 2003. Assessing pre-and post-deformation in the southern Arava Valley segment of the Dead Sea Transform, Israel by differential interferometry. *Remote Sens. Environ.* **86**: 141-149.

Salvany JM, García-Veigas J, Ortí F. 2007. Glauberite-halite association of the Zaragoza Gypsum Formation (Lower Miocene, Ebro Basin, NE Spain). *Sedimentology* **54**: 443-467.

Sástago C. 1796. Descripción de los canales Imperial de Aragón y Real de Tauste. Ministerio de Fomento, Madrid, 174 p.

Scharroo R, Visser P. 1998. Precise orbit determination and gravity field improvement for the ERS satellites. *J. Geophys. Res.-Oceans* **103**: 8113-8127.

Sigmudsson F, Durand P, Massonnet D. 1999. Opening of an eruptive fissure and seaward displacement at Piton de la Fournaise volcano measured by Radarsat satellite radar interferometry. *Geophys. Res. Lett.* **26**: 533-536.

Soriano MA, Simón JL. 1995. Alluvial dolines in the central Ebro basin, Spain: a spatial and developmental hazard analysis. *Geomorphology* **11**: 295-309.

Soriano MA, Simón JL. 2002. Subsidence rates and urban damages in alluvial dolines of the central Ebro Basin (NE Spain). *Environ. Geol.* **42**: 476-484.

Stramondo S, Saroli M, Tolomei C, Moro M, Doumaz F, Pesci A, Loddo F, Baldi P, Boshi E. 2007. Surface movements in Bologna (Po Plain-Italy) detected by multitemporal DInSAR. *Remote Sens. Environ.* **110**: 304-316.

Tarayre H, Massonet D. 1996. Atmospheric propagation heterogeneities revealed by ERS-1 interferometry. *Geophys. Res. Lett.* **23**: 989-992.

Tizzani P, Berardino P, Casu F, Euillades P, Manzo M, Ricciardi GP, Zeni G, Lanari R. 2007. Surface deformation of Long Valley caldera and Mono Basin, California, investigated with the SBAS-InSAR approach. *Remote Sens. Environ.* **108**: 277-289.

Torrescusa S, Klimowitz J. 1990. Contribución al conocimiento de las evaporitas Miocenas (Formación Zaragoza) de la Cuenca del Ebro. In: Ortí, F. and Salvany, J.M. (Eds.). Formaciones evaporíticas de la Cuenca del Ebro y cadenas periféricas y de la zona de Levante, ENRESA-GPG, Barcelona, 120-122.

Usai S. 2003. A Least Squares Database Approach for SAR Interferometric Data. *IEEE Trans. Geosci. Remote Sens.* **41**: 753-760.

Waltham AC. 1989. Ground subsidence, Blackie, Glasgow, 202 p.

Wdowinksky S, Kim SW, Amelung F, Dixon T, Miralles-Wilhelm F, Sonenshein R. 2008. Space-based detection of wetlands'surface water level changes from L-band SAR interferometry. *Remote Sens. Environ*. **112**: 681-696.

Werner C, Wegmuller U, Strozzi T, Wiesmann A. 2003. Interferometric point target analysis for deformation mapping, International Geoscience and Remote Sensing Symposium (IGARSS 2003) **7**: 4362-4364.

Zebker H, Villasenor J. 1992. Decorrelation in interferometric radar echoes. *IEEE Trans. Geosci. Remote Sens*. **30**: 950-959.

Figure captions

Figure 1. Geographic location and digital elevation model of the study area showing the main geomorphic features and villages indicated in the text.

Figure 2. A: Active multiple rotational landslide with lateral spreading component in the gypsum escarpment located downstream of Zaragoza city. B: Building destroyed by a rock-fall in October 2002 fallen from the gypsum escarpment located upstream of Zaragoza city (outskirts of Alfocea village).

Figure 3. DInSAR mean deformation velocity map for the 1995-2000 time span overlying a Landsat ETM+ image (band 4) from August 2000. The location of the reference point assumed as stable (asterisk) and the analyzed deformation sites are also shown. Negative and positive values indicate subsidence and uplift, respectively.

Figure 4. A: SBAS DInSAR ground deformation map of site 1 on an orthophotograph from 2000. B: Image taken in 1927 showing wetlands hosted in sinkholes (arrows) that have been filled and developed. The large sinkhole situated to the right is now overlain by the El Portazgo Industrial State. C: Geomorphological map of site 1 showing the distribution of sinkholes and the measured mean subsidence rates. D: Active Subsidence depression in El Portazgo Industrial State. The building situated at this site was demolished due to subsidence damage (Photograph taken in June 1996).

Figure 5. DInSAR LOS deformation time series in sinkhole sites and mean daily rainfall (mm/day) obtained from the Zaragoza Airport weather station precipitation record.

Figure 6. A: SBAS DInSAR ground deformation map of site 2 on an orthophotograph from 2000. B: Image of site 2 taken in 1956 revealing that the area affected by subsidence coincides with a large sinkhole.

Figure 7. A: SBAS DInSAR ground deformation map of site 3 depicted on an orthophotograph from 2000. B: Geomorphological map of site 3 showing the distribution of active landslides. C: Oblique aerial view of active landslide in site 3. See location in B. D. SBAS DInSAR ground deformation map of site 4 depicted on an orthophotograph from 2000.

Figure 8. DInSAR LOS deformation time series in landslide sites and mean daily rainfall (mm/day) obtained for the Remolinos weather station precipitation record.

Figure 9. A: SBAS DInSAR ground deformation map of site 5 depicted on an orthophotograph from 2000. B: Geomorphological map of site 5 showing the distribution of landslides and the María del Carmen mine. C: Oblique aerial view of active landslide. See location in B. D. Reactivated landslide occurred on July 7, 2004 at the entrance of María del Carmen mine trapping a truck. The DInSAR analysis indicates deformation in this landslide previous to its catastrophic collapse.

Figure 10. DInSAR LOS deformation time series in the María del Carmen salt mine and mean daily rainfall between radar dates obtained from the precipitation record of Remolinos weather station located at about 1.5 km from the mine.

Table 1. Sensor, date and orbit number of the SAR images selected for this study. The indicated temporal interval is referred to the date of the oldest image.

Sensor	Date	Orbit number	Number of days from the first date
ERS-1	05/07/1995	20,766	0
ERS-2	10/08/1995	1,594	36
ERS-2	14/09/1995	2,095	71
ERS-1	10/04/1996	24,774	280
ERS-2	20/06/1996	6,103	351
ERS-2	29/08/1996	7,105	421
ERS-2	03/10/1996	7,606	456
ERS-2	12/12/1996	8,608	526
ERS-2	20/02/1997	9,610	596
ERS-2	27/03/1997	10,111	631
ERS-2	01/05/1997	10,612	666
ERS-2	10/07/1997	11,614	736
ERS-2	18/09/1997	12,616	806
ERS-2	27/11/1997	13,618	876
ERS-2	05/02/1998	14,620	946
ERS-2	03/09/1998	17,626	1156
ERS-2	01/04/1999	20,632	1366
ERS-2	10/06/1999	21,634	1436
ERS-1	14/07/1999	41,808	1470
ERS-1	27/01/1999	43,311	1575
ERS-2	28/10/1999	23,638	1576
ERS-2	06/01/2000	24,640	1646
ERS-1	09/02/2000	44,814	1680
ERS-2	16/03/2000	25,642	1716
ERS-2	03/08/2000	27,646	1856
ERS-2	12/10/2000	28,648	1926
ERS-2	21/12/2000	29,650	1996

978 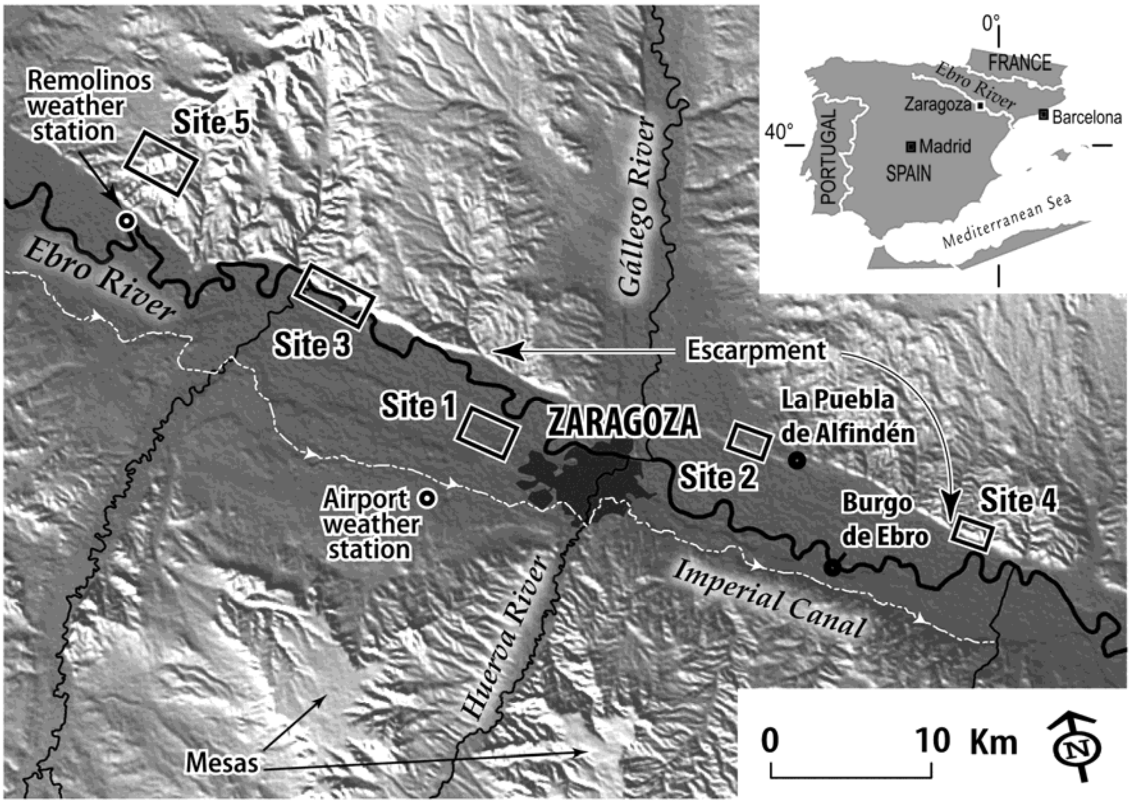
Remolinos
weather
station
Site 5
Ebro River
Site 3
Gállego River
Escarpment
Site 1
ZARAGOZA
La Puebla
de Alfindén
Site 2
Airport
weather
station
Burgo
de Ebro
Site 4
Imperial Canal
Huerva River
Mesas
0
10 Km
N
0°
FRANCE
Ebro River
Zaragoza
Barcelona
40°
PORTUGAL
Madrid
SPAIN
Mediterranean Sea

979

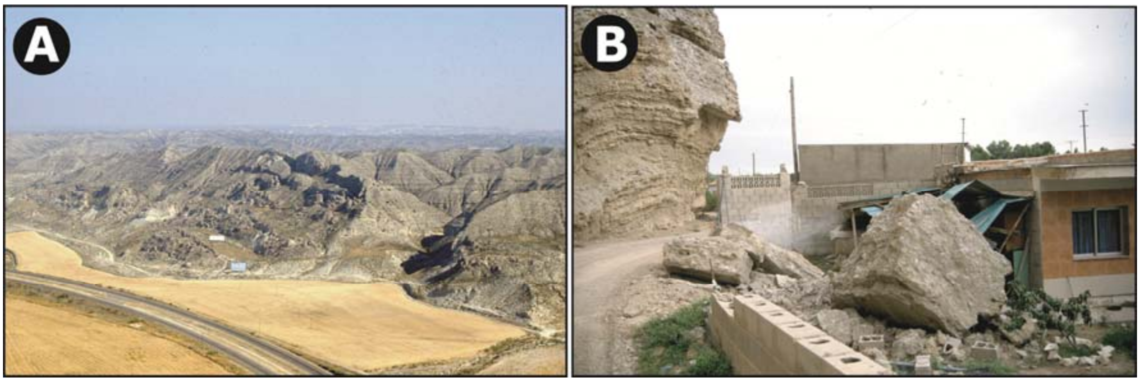
A
B

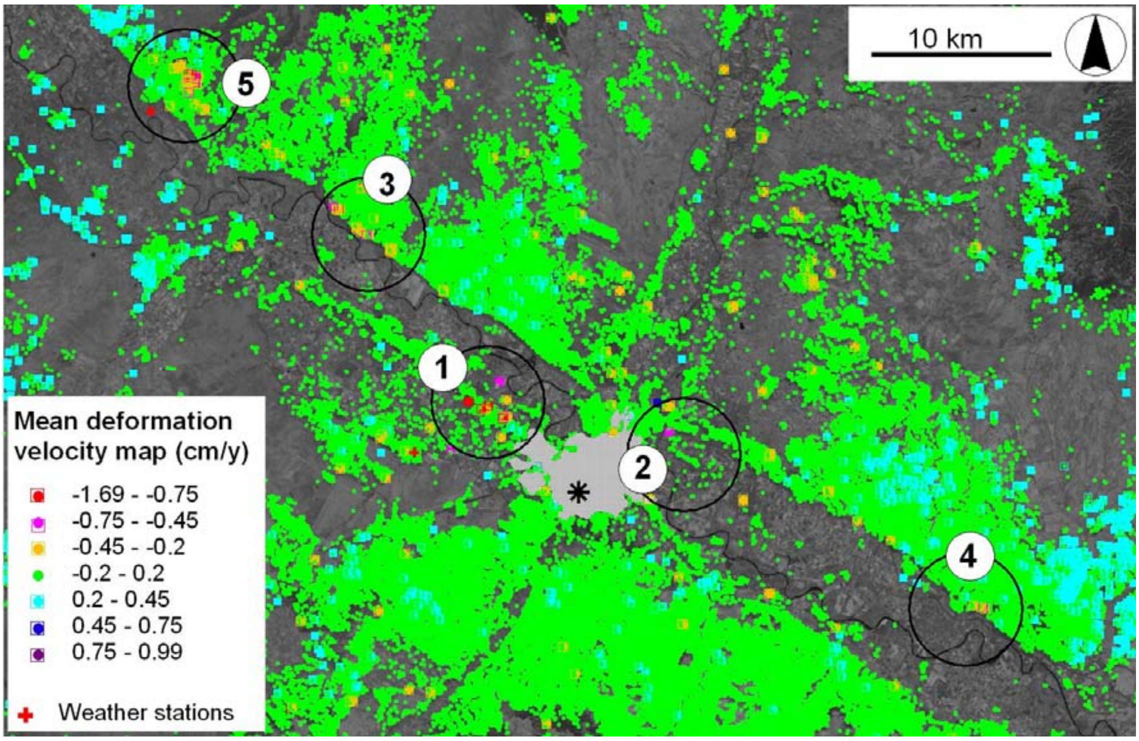
10 km
5
3
1
2
4
Mean deformation velocity map (cm/y)
-1.69 - -0.75
-0.75 - -0.45
-0.45 - -0.2
-0.2 - 0.2
0.2 - 0.45
0.45 - 0.75
0.75 - 0.99
Weather stations

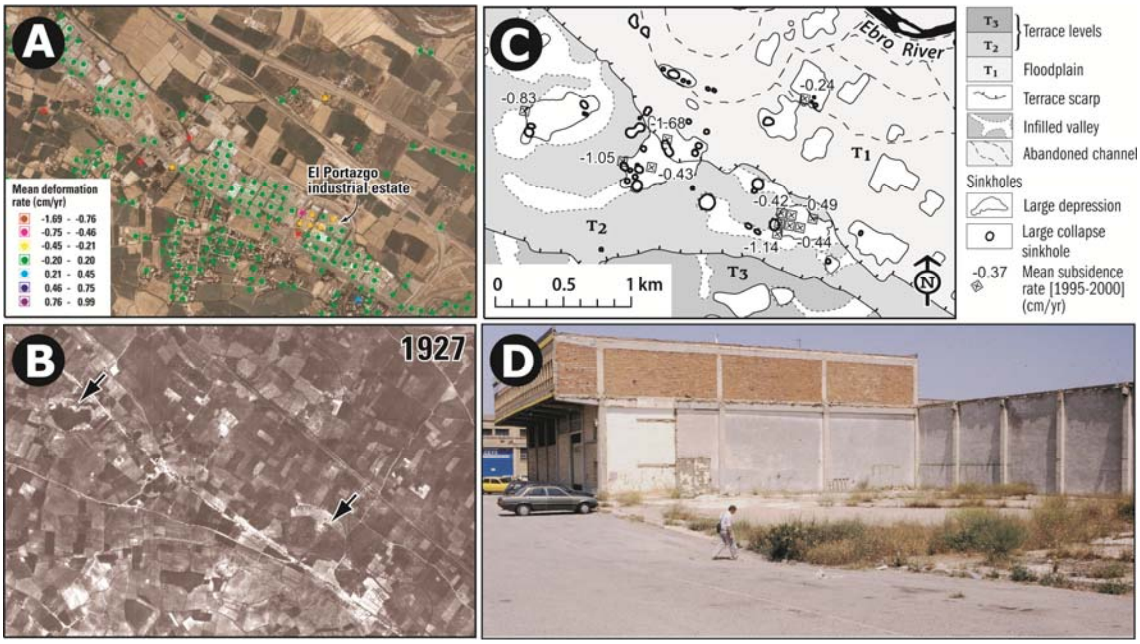
A
Mean deformation rate (cm/yr)
-1.69 - -0.76
-0.75 - -0.46
-0.45 - -0.21
-0.20 - 0.20
0.21 - 0.45
0.46 - 0.75
0.76 - 0.99
El Portazgo industrial estate
B
1927
C
Ebro River
-0.83
-1.68
-0.24
-1.05
-0.43
T1
-0.42
-0.49
T2
-1.14
-0.44
T3
0 0.5 1 km
N
T3
T2
Terrace levels
T1
Floodplain
Terrace scarp
Infilled valley
Abandoned channel
Sinkholes
Large depression
Large collapse sinkhole
-0.37
Mean subsidence rate [1995-2000] (cm/yr)
D

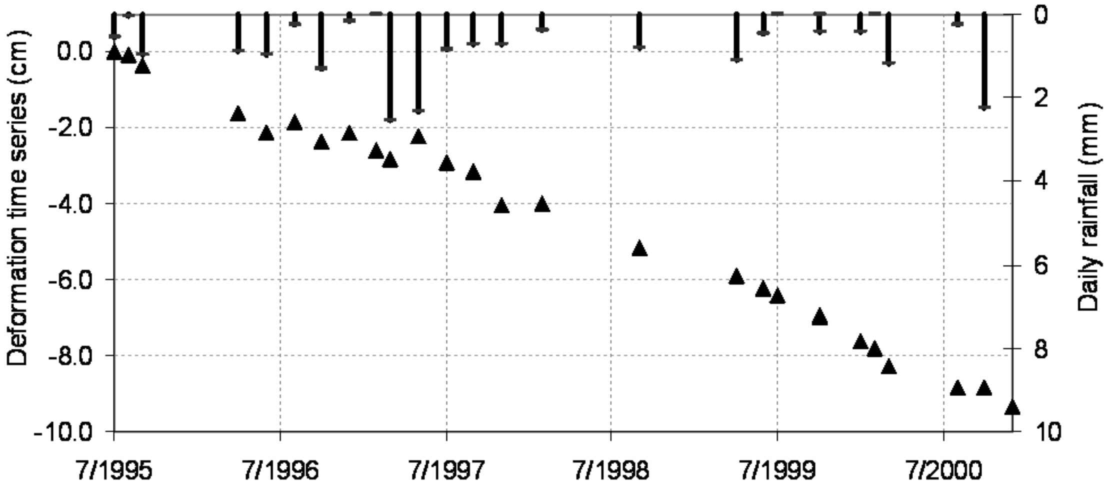
Deformation time series (cm)
0.0
-2.0
-4.0
-6.0
-8.0
-10.0
Daily rainfall (mm)
0
2
4
6
8
10
7/1995
7/1996
7/1997
7/1998
7/1999
7/2000

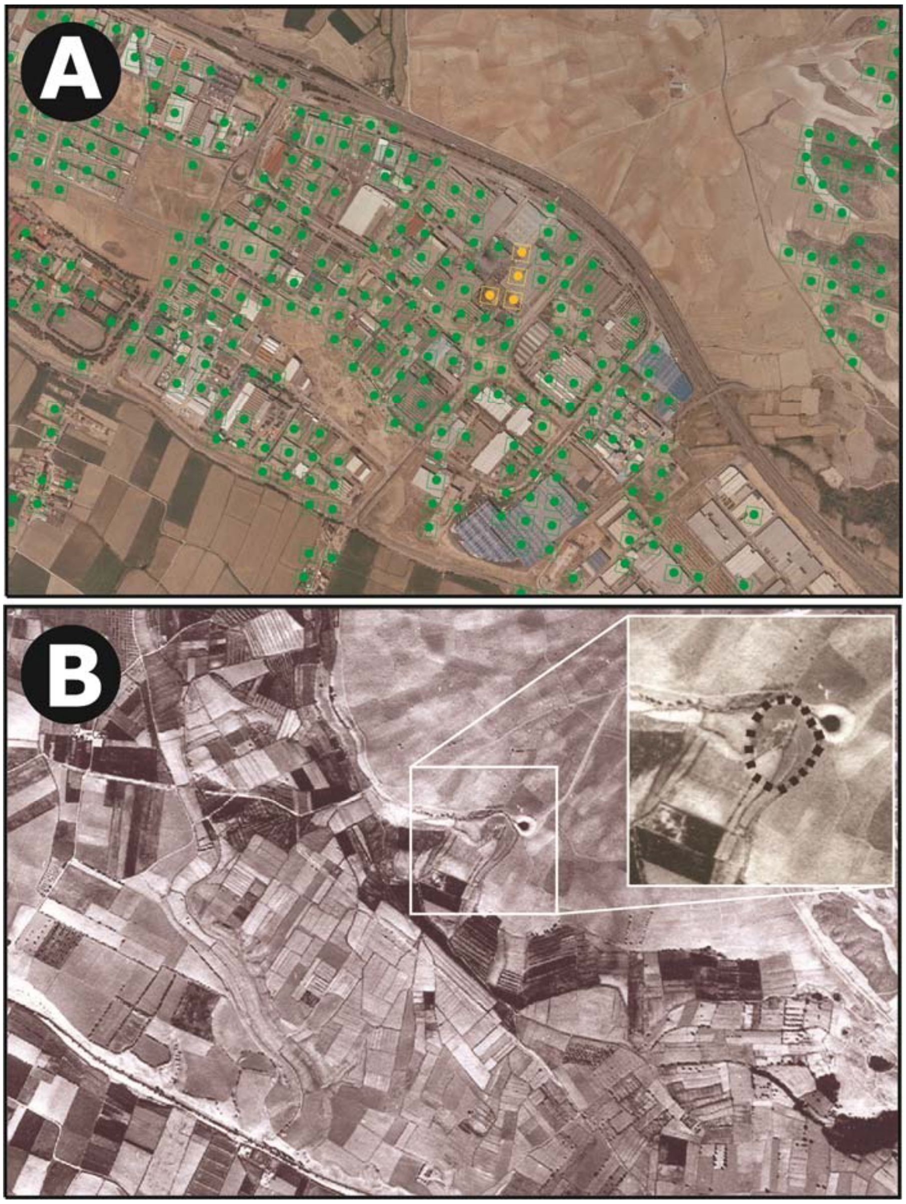

989

990

991 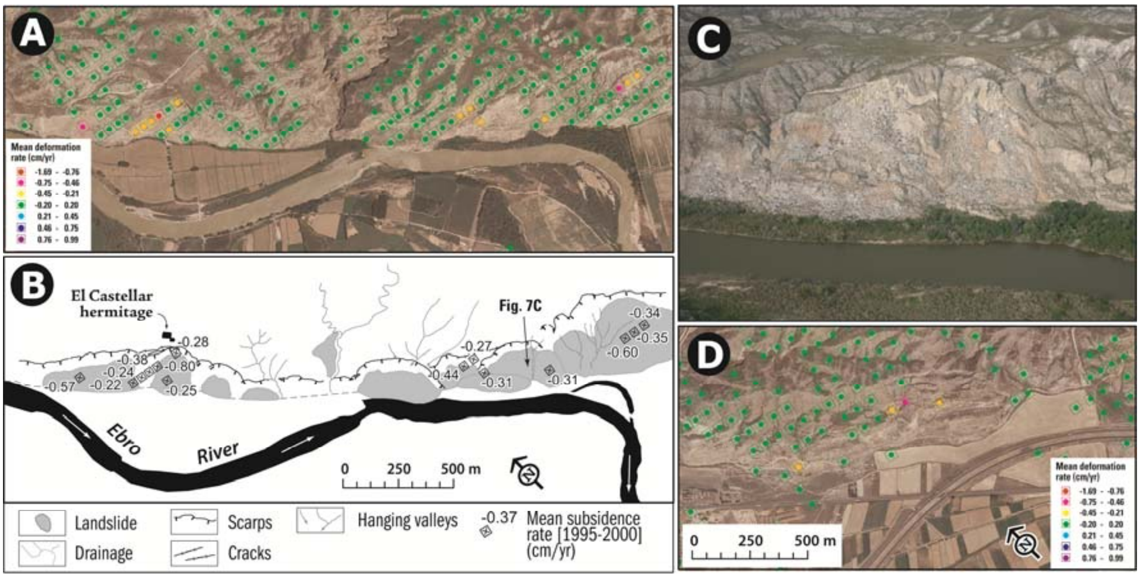
A
Mean deformation rate (cm/yr)
-1.69 - -0.76
-0.75 - -0.46
-0.45 - -0.21
-0.20 - 0.20
0.21 - 0.45
0.46 - 0.75
0.76 - 0.99
B
El Castellar hermitage
-0.28
-0.38
-0.24
-0.80
-0.57
-0.22
-0.25
Fig. 7C
-0.34
-0.35
-0.60
-0.27
-0.44
-0.31
-0.31
Ebro
River
0 250 500 m
Landslide
Drainage
Scarps
Cracks
Hanging valleys
-0.37 Mean subsidence rate [1995-2000] (cm/yr)
C
D
Mean deformation rate (cm/yr)
-1.69 - -0.76
-0.75 - -0.46
-0.45 - -0.21
-0.20 - 0.20
0.21 - 0.45
0.46 - 0.75
0.76 - 0.99
0 250 500 m

992

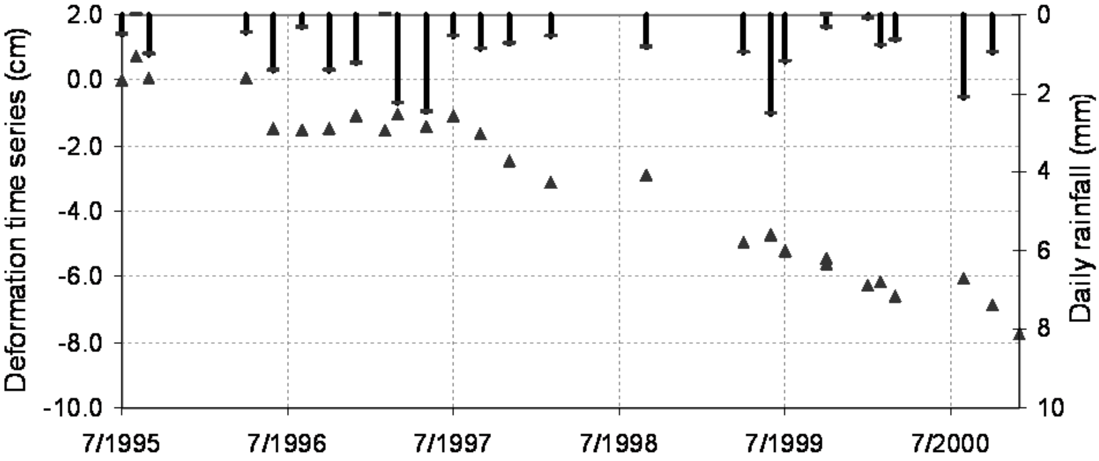

Deformation time series (cm)
2.0
0.0
-2.0
-4.0
-6.0
-8.0
-10.0
Daily rainfall (mm)
0
2
4
6
8
10
7/1995
7/1996
7/1997
7/1998
7/1999
7/2000

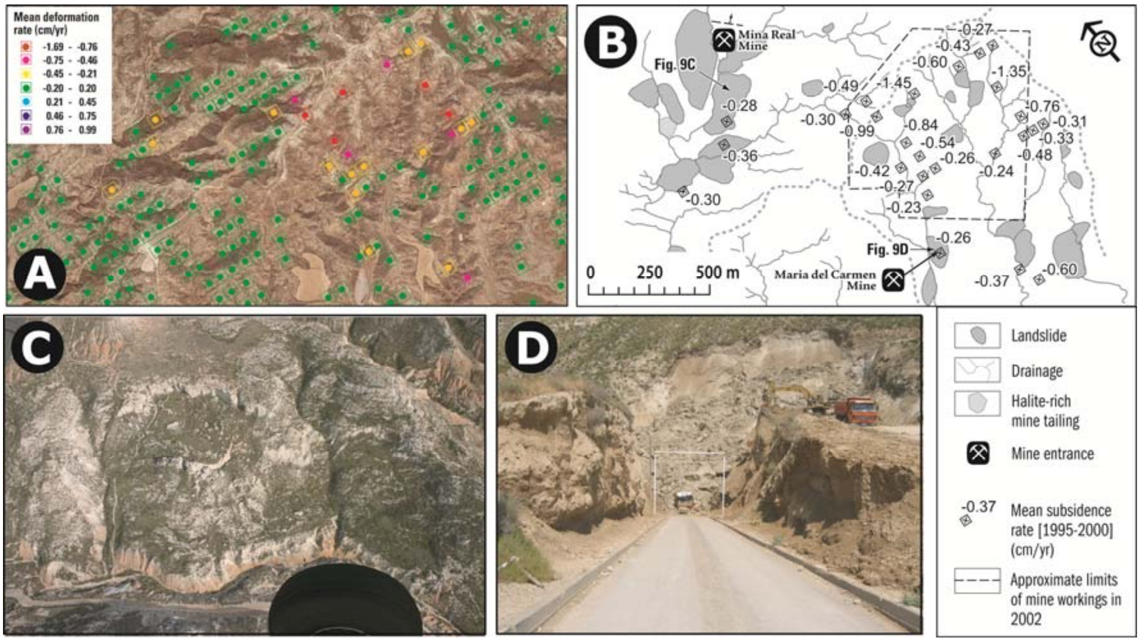

Mean deformation rate (cm/yr)
-1.69 - -0.76
-0.75 - -0.46
-0.45 - -0.21
-0.20 - 0.20
0.21 - 0.45
0.46 - 0.75
0.76 - 0.99
A
B
Mina Real Mine
Fig. 9C
Fig. 9D
Maria del Carmen Mine
0
250
500 m
-0.27
-0.43
-0.60
-1.35
-0.49
-1.45
-0.28
-0.30
-0.99
-0.76
-0.31
-0.33
-0.84
-0.54
-0.48
-0.36
-0.26
-0.42
-0.24
-0.27
-0.30
-0.23
-0.26
-0.37
-0.60
C
D
Landslide
Drainage
Halite-rich mine tailing
Mine entrance
-0.37
Mean subsidence rate [1995-2000] (cm/yr)
Approximate limits of mine workings in 2002

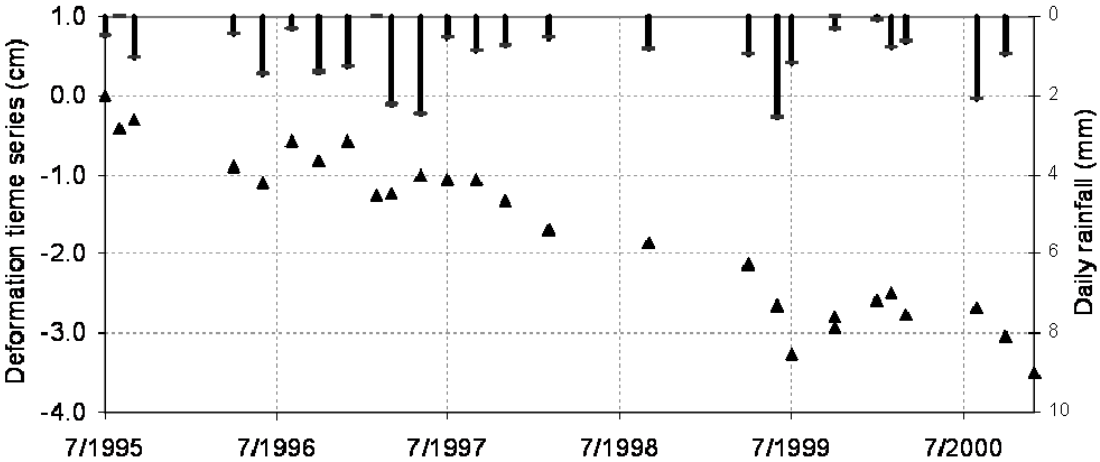

Deformation tieme series (cm)
1.0
0.0
-1.0
-2.0
-3.0
-4.0
7/1995
7/1996
7/1997
7/1998
7/1999
7/2000
Daily rainfall (mm)
0
2
4
6
8
10

997